JOURNAL OF GEOPHYSICAL RESEARCH, VOL. 105, NO. C8, PAGES 19,515–19,534, AUGUST 15, 2000

Sea surface velocities from sea surface temperature image sequences
2. Application to the Brazil-Malvinas Confluence area

Xavier Vigan[1]

Laboratoire d'Océanographie Physique, Muséum National d'Histoire Naturelle, Paris

Christine Provost

Laboratoire d'Océanographie Dynamique et de Climatologie, Centre National de la Recherche Scientifique, Paris

Guillermo Podesta

Rosentiel School of Marine and Atmospheric Sciences, University of Miami, Miami, Florida

Abstract. An inverse variational model is applied to four exceptionally cloud-free sea surface temperature image sequences of the Brazil-Malvinas Confluence area for the purpose of estimating sea surface velocity fields. The velocity fields are constructed by minimizing a mixed layer integrated form of the heat balance equation while the horizontal divergence and vorticity of the flow field are controlled. The source terms involved in the heat balance are determined by fitting a polynomial to diurnal temperature variations as a function of temperature and longitude. A sensitivity study of the solution to perturbations of the weights imposed to the constraints on divergence and vorticity as well as of the representation of the source terms yields error fields associated with the velocity. A comparison of the estimated velocity fields with available concomitant *in situ* velocity measurements shows that the fields are realistic. Errors are of the order of 15-20% in magnitude and 20°-25° in direction. These errors fall within the error bars of 25-30% in magnitude and of 30°-35° in direction, except for the summer image series. Surface velocities of 0.5-0.6 m s^{-1} are obtained across the Malvinas Current. They are > 1 m s^{-1} in the frontal region, in the Brazil Current overshoot, and in warm and cold core rings and vary between 0.3 and 0.8 m s^{-1} in the Brazil Current. With some hypotheses on the vertical shear of the horizontal flow the transport of the Malvinas Current is estimated to be $25 \pm 5\, Sv$ between 41° and 40°S.

1. Introduction

Sea surface dynamics in the southwest Atlantic Ocean are dominated by the confluence of the warm and salty Brazil Current (BC) and the cold and fresher Malvinas Current (MC). Surface velocities > 1 m s^{-1} have been observed [*Olson et al.*, 1988]. The presence of several fronts and eddies makes the area a complex one to describe. *In situ* surface velocity measurements are difficult to obtain in the area because of rough weather conditions. Few surface velocity measurements, only a few buoys [*Olson et al.*, 1988; *Kartavtseff*, 1996], floats [*Lourenço*, 1997] and a ship-mounted ADCP transect [*Saunders and King*, 1994] have been reported in the literature.

Sea surface temperature (SST) images provide a synoptic view of the ocean several times a day with a high spatial resolution. The animation of SST image sequences of the confluence suggests that the ocean is not at rest and that one would like to estimate sea surface velocities from the apparent motion of structures observable in the images. *Vigan et al.* [this issue] cite the various methods used and test the inversion of the heat balance equation method originally proposed by *Kelly* [1989] on outputs of a primitive equation oceanic model. A flow field is sought that minimizes the following cost function:

$$\mathcal{H}_1 = \left(\frac{\partial T}{\partial t} + \mathbf{u}\nabla T - S\right)^2 + \alpha^2 (\nabla \cdot \mathbf{u})^2 + \beta^2 (\nabla \times \mathbf{u})^2, \quad (1)$$

[1]Now at Laboratoire d'Océanographie Dynamique et de Climatologie, Centre National d'Études Spatiales, Paris.

Paper number 2000JC900028.
0148-0227/00/2000JC900028$09.00

where T is the temperature of the mixed layer, $\mathbf{u}$ is the horizontal velocity at the surface, and S is an SST source term. Here α and β are penalty coefficients that govern the influence of the constraints on the solution. Among an infinite number of solutions obtained by varying α and β a family of velocity fields is selected by setting a threshold on the misfit of the heat balance defined as $\epsilon = \sum(\partial_t T + \mathbf{u}\nabla T - S)^2 / \sum(\partial_t T)^2$. The average velocity is compared to the "true" velocity field from the Miami Isopycnic Coordinate Oceanic Model (MICOM). The rms differences between the inverted and the MICOM velocities are 11% in magnitude and 17° in direction. These errors are assumed to be due on one hand, to the fact that the source terms are neglected and on the other hand, to the fact that flow field components proportional to the thermal wind are forced to zero by the inverse model. Error fields associated with the velocity estimates are also computed through a sensitivity study. Differences between the inverted and the MICOM velocities fall below the error estimates, except over regions where temperature variations from one image to the next are zero.

Here we invert exceptionally cloud-free SST image sequences of the Brazil-Malvinas Confluence region during year 1995. An additional difficulty compared to model output inversions is the estimation of the term S in (1) encompassing heat fluxes and entrainment. In the second section we present the image sequences as well as concomitant available *in situ* velocity measurements. We then propose two ways of estimating the source term of the heat balance. Results from the inversions are presented in section 4 along with the associated error fields. The velocities are compared to the *in situ* data and discussed in section 5.

2. The data

2.1. High Resolution Sea Surface Temperature Images

The satellite-derived SST fields used in this study are based on data collected by the advanced very high resolution radiometer AVHRR, an infrared radiometer flying aboard polar-orbiting spacecraft of the National Oceanic and Atmospheric Administration (NOAA) series. SST was computed using a multichannel algorithm for AVHRR channels 4 and 5 [*McClain et al.*, 1985].

The correct geolocation of pixels on the image series is important for the accuracy of the method. One of the main sources of errors in geolocation is drift in the spacecraft clock. This was corrected using a look-up table of clock drift. Errors in pixel location due to spacecraft attitude (roll, pitch, and yaw) were corrected by matching coastlines in the images with an accurate digital coastline database. These corrections together result in subpixel accuracy geolocation [*Emery et al.*, 1989].

The original high-resolution data (1.1 km at nadir) were then remapped to a fixed Earth-based grid using a cylindrical equirectangular projection with a nominal resolution of about 4 km. After the remapping a given pixel represents the same geographic location on every image in the series.

Among 838 images spanning the period from February 1 to December 31, 1995, only 27 are retained. The others cannot be used because of cloud cover. There are two criteria for selecting series of images: meteorological conditions (no cloud cover and presence of wind) and the number of successive images verifying the first criterion. Table 1 describes the images that were selected. Columns 1-6 present the image reference, the day and time of acquisition (GMT), the time step between consecutive images, observable structures, and the availability of concomitant *in situ* velocity measurements. The precision of the time of acquisition is a few minutes. No *in situ* velocity measurements are available for the B series. The presence of clouds on the image series selected is detected in two steps: temperatures < 2°C are flagged as clouds, and the remaining are detected subjectively.

Four SST images extracted from series A, B, C, and D of Table 1 are shown in Plate 1. Some oceanic patterns are common to the four series. The MC is found toward the southwest of the area (with surface temperatures of 4°-5°C during winter and 9°-11°C during summer). The warmer BC is observed to the north (20°C during winter and 24°-28°C during summer). Both currents meet between 36° and 40°S offshore of the Rio de la Plata estuary. After the confluence a larger part of the MC water returns to the south, while the BC overshoots as far south as 47°S, where coherent vortex patterns are often observed.

Each series reveals peculiar features on which we focus (white squares of Plate 1). The A series (Plate 2a) is typical of the region where both currents meet at 38°S to form a jet to the southeast of the confluence. The B series (Plate 2b) exhibits that the spectacular warm-core eddy Léon centered at (45.5°S, 55.5°W) with a diameter of ~160 km (average of the larger and smaller axes on image B_1) pinched off the BC overshoot as described by *Hooker and Brown* [1996]. Léon is accompanied by two smaller eddies to the southeast centered at (47.5°S, 54°W) and (47°S, 53.5°W), while temperatures are in the range 4°-6°C and 10°-12°C, respectively. Filaments are ejected into the saddle point regions between these three eddies. In Plate 2c a large BC meander, the temperature of which is ~20°C, overshoots to the south. Plate 2d shows BC water extending from the northeast to the southwest of the region, with temperatures of about ~18°C. West of the BC, the continental shelf waters have temperatures of 8°-12°C. Cold-core eddy Jules (D series) is observed at (36.5°S, 47.5°W)

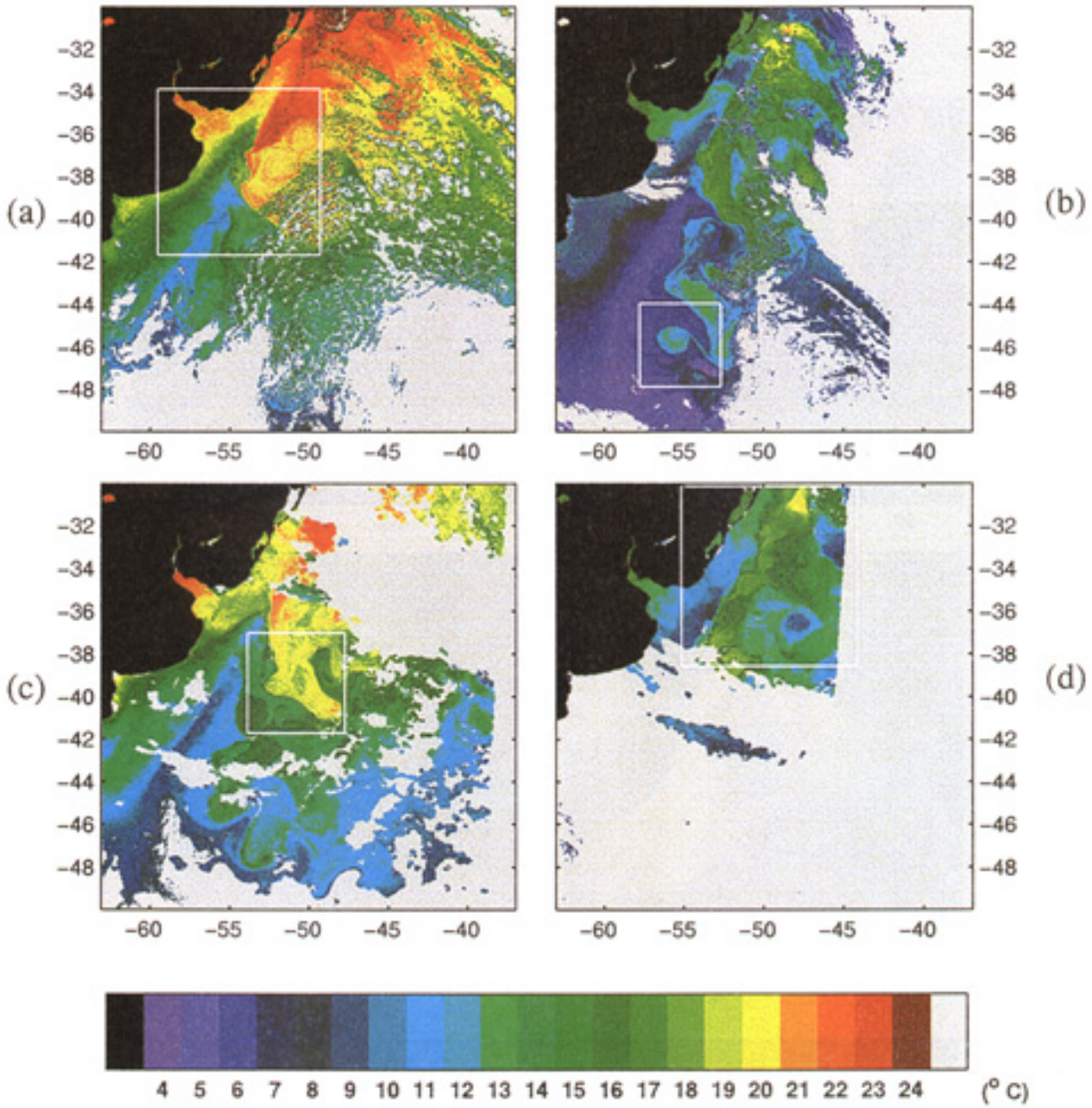

Plate 1. (a) Sea surface temperature (SST) image of the A series showing a summer situation of the area on March 10, 1995. The Brazil Current (BC) (red) meets the colder Malvinas Current (MC) (blue) at ~38°S offshore of the Rio de la Plata river estuary. (b) SST image of the B series (September 27, 1995) exhibiting warm core eddy Léon. (c) SST image of the C series (December 2, 1995) showing a large eddy detaching from the BC overshoot at ~40°S. (d) SST image spanning the cold-core eddy Jules event (September 7, 1995).

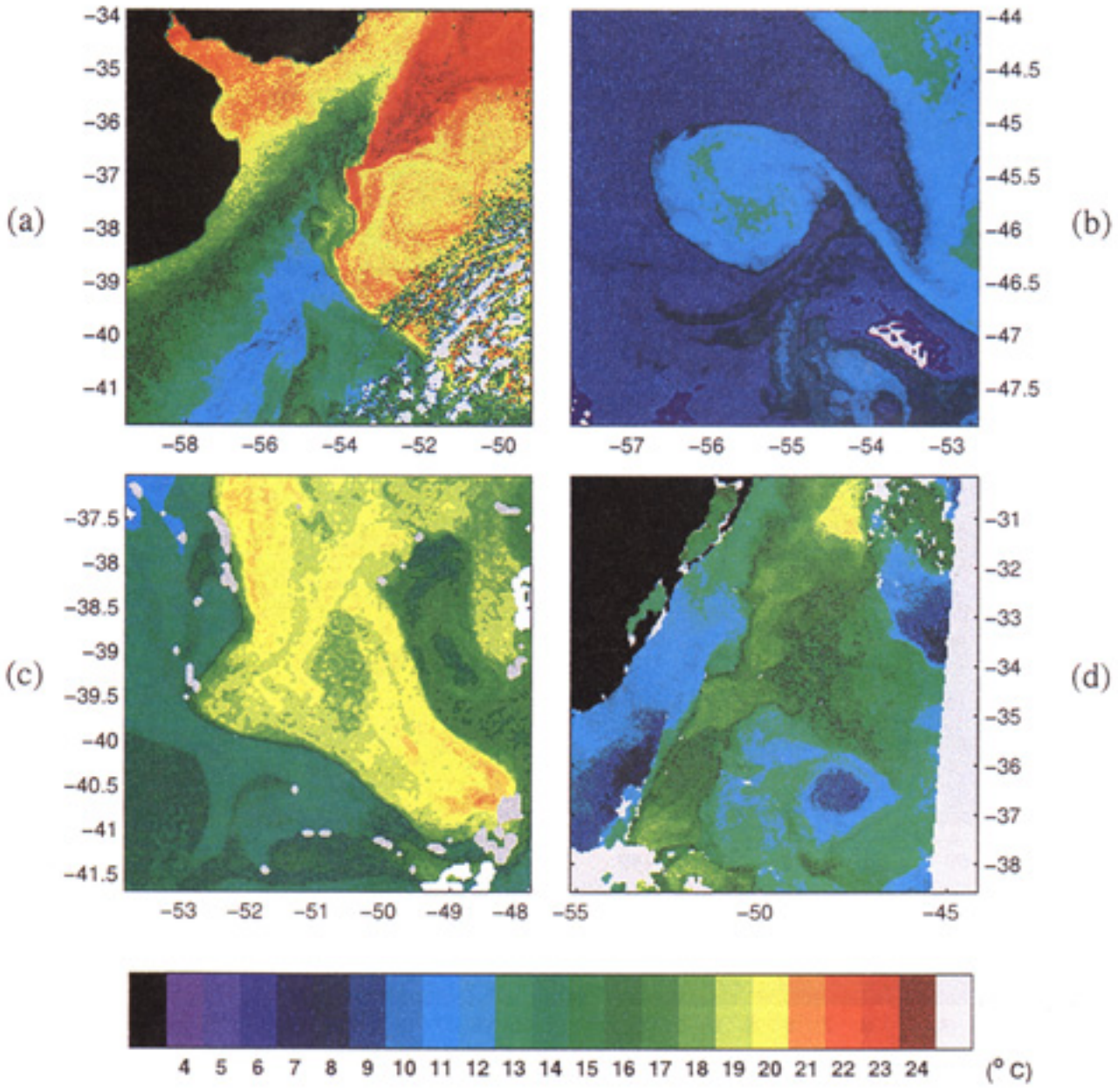

Plate 2. (a) The 800x800 km subarea of Plate 1a centered on the confluence. (b) The 400x400 km subarea of Plate 1b centered on warm core eddy Léon. (c) The 500x500 km subarea of Plate 1c centered on the principal meander of the Brazil Current. (d) The 870x870 km subarea of Plate 1d featuring the Brazil Current and cold core eddy Jules.

Table 1. (A, B, C, and D) Image Series Used in the Inversions

Reference	Day	Time, UT	δt	Observed Structures	*In Situ* Data
A_1	March 9, 1995	1842	-	MC/BC/front	CMM
A_2	March 10, 1995	0425	09 hours 17 min	MC/BC/front	CMM
A_3	March 10, 1995	1830	14 hours 05 min	MC/BC/front	CMM
A_4	March 11, 1995	0555	11 hours 25 min	MC/BC/front	CMM
A_5	March 11, 1995	1819	12 hours 24 min	MC/BC/front	CMM
A_6	March 12, 1995	0545	11 hours 26 min	MC/BC/front	CMM
A_7	March 12, 1995	1809	13 hours 00 min	MC/BC/front	-
B_1	Sept. 27, 1995	0506	-	WCR Léon	altimetry
B_2	Sept. 27, 1995	1732	12 hours 25 min	WCR Léon	altimetry
B_3	Sept. 28, 1995	0455	09 hours 39 min	WCR Léon	altimetry
B_4	Sept. 28, 1995	1721	12 hours 26 min	WCR Léon	-
B_5	Sept. 29, 1995	1711	22 hours 06 min	WCR Léon	-
B_6	Sept. 30, 1995	0434	09 hours 41 min	WCR Léon	-
B_7	Sept. 30, 1995	1841	14 hours 06 min	WCR Léon	-
B_8	Oct. 1, 1995	0423	09 hours 42 min	WCR Léon	-
C_1	Nov. 28, 1995	1805	-	overshoot	buoys/floats
C_2	Nov. 29, 1995	0529	11 hours 24 min	overshoot	buoys/floats
C_3	Nov. 29, 1995	1754	12 hours 25 min	overshoot	buoys/floats
C_4	Nov. 30, 1995	0344	09 hours 50 min	overshoot	buoys/floats
C_5	Nov. 30, 1995	1743	12 hours 25 min	overshoot	buoys/floats
C_6	Dec. 1, 1995	1733	23 hours 50 min	overshoot	buoys/floats
C_7	Dec. 2, 1995	0456	11 hours 23 min	overshoot	buoys/floats
C_8	Dec. 2, 1995	1723	12 hours 27 min	overshoot	buoys/floats
C_9	Dec. 3, 1995	0447	11 hours 24 min	overshoot	buoys/floats
D_1	Sept. 7, 1995	0458	-	CCR Jules	buoys/floats
D_2	Sept. 7, 1995	1732	12 hours 34 min	CCR Jules	buoys/floats
D_3	Sept. 8, 1995	0502	11 hours 30 min	CCR Jules	buoys/floats

The times of acquisition are given with the precision of a few minutes. The features observed and *in situ* concomitant data available are given in the last two columns, warm-core rings (WCR), cold-core rings (CCR), and currentmeter mooring (CMM).

with a diameter of ~170 km (Plate 2d). That last series is the only winter situation from which inversions can be performed because of the prevalence of clouds during that period of the year.

2.2. In situ Velocity Measurements

Three types of *in situ* observations are used for a comparison to the velocity estimates: current meters deployed during the confluence experiment, Marisonde buoys, and RAFOS floats. Current meters were deployed during December 1993 and were recovered at the end of June 1995 (Plate 3a) *Vivier and Provost* [1999a]. The data are simultaneous to the A image series spanning the end of summer 1995. Five Marisonde buoys equipped with 150 m long thermistor chains were deployed on June 25, 1995, at (36°S, 53°W) [*Kartavtseff*, 1996]. The Argos system reports positions every ~ 1 hour and 45 minutes, but there are gaps of several hours between passes. The spatial precision of the positioning is better than 1 km. Trajectories (Plate 3b) are concomitant to the B, C, and D image series. We use the surface trajectories provided by nine RAFOS floats [*Lourenço*, 1997], which surfaced on November 20, 1995, at the end of their mission and transmitted their surface position (Plate 3c). The five Marisonde trajectories as well as the nine RAFOS floats are resampled every hour. The three sets of *in situ* data are low pass-filtered with a 12 hour cutoff corresponding approximately to the time step between successive images.

3. Source Terms

The term S involved in the heat balance represents contributions of surface heat fluxes at the surface of the ocean as well as entrainment at the base of the mixed layer [*Vigan et al.*, this issue]. Their contribution to the heat balance is neglected in the inversions of Vigan et al. and taken into account in the computation of the error bars. However, heat fluxes can be very large in some situations, especially during periods of strong insolation and in the absence of wind [*Cornillon and Stramma*, 1985]. The signature of heat fluxes on SST constitutes an issue with regard to a quantitative use

of satellite images. Decorrelating the contribution of heat fluxes and entrainment to that due to advection in $\partial T/\partial t$ represents a crucial problem to estimating velocity fields from image sequences. In the following we propose and compare two approaches to represent the source term.

3.1. Large-Scale Representation

A first approach is to suppose that the evolution of temperature at the surface of the ocean due to air-sea heat fluxes and entrainment exhibits large spatial scales because typical scales of atmospheric forcing are large. *Stramma et al.* [1986] observe in the Sargasso Sea that the spatial extent of diurnal SST warming events are well correlated with the spatial extent of the atmospheric pressure field. Regarding temperature variations from image D_1 to D_2 (Plate 4c), we observe a strong variability at small scales (5-20 km), from -2° to 4°C. We also observe larger-scale temperature variations of ~0.5°C across the BC and of 1° to 1.5°C over the subtropical waters to the southeast. Variations are very large over the continental shelf and over the cold-core eddy of the order of 2°C. In the power spectral density of $\partial T/\partial t$ (Plate 4d) a series of peaks between 4 and 90 km and another peak at ~ 250 km suggest a scale separation. Since the images are separated by a 12 hour time step, the energy observed at 250 km cannot be due to advection. We attribute temperature variations at these scales to air-sea surface heat fluxes as well as to entrainment at the base of the mixed layer due to the wind stress at the surface. These two contributions cannot be decorrelated in the sense that they both stem from a large-scale forcing, the effect of which on the SST are indiscernible. A first approach to representing the source terms of the heat balance is to apply a low-pass filter to $\partial T/\partial t$ the cutoff of which is set here to 90 km. In the S field obtained in this way (Plate 4e) the Brazil waters warm up by ~0.8°C, and the subtropical waters warm up by 1°-2°C. The cold-core eddy and the continental shelf waters exhibit temperature variations of up to 2°C. We thus attribute $\partial T/\partial t - S$ (Plate 4f) to temperature variations due to advection.

3.2. Representation As a Function of Temperature

Representing heat fluxes by a large-scale term is realistic from the point of view of the atmosphere, where typical scales are larger than 100 km. However, the SST images presented here reveal a strong variability at much smaller scales: the existence of large horizontal temperature gradients is necessarily associated with strong horizontal gradients in the heat flux contribution to the source terms because latent, infrared, and sensible fluxes are functions of the SST. For the purpose of taking into account smaller scales also in the representation of the source terms we attempt to model S as a function of the SST. Plate 5a suggests the fit of a polynomial law to represent S as a function of temperature. For that purpose we minimize the functional $\mathcal{G}$:

$$\mathcal{G}(T) = \left[\left(\frac{\partial T}{\partial t}\right) - \sum_{k=0}^{10} a_k T^k\right]^2, \qquad (2)$$

where a_k are the polynomial coefficients. We choose a polynomial of order 10 because increasing the degree to more than 10 does not improve the fit, in the sense that $\mathcal{G}(T)$ reaches a minimum for a polynomial of degree 10. One can observe in the resulting S field (Plate 5b) a general warming of the region from 0.3°C for the Brazil waters to 2°C for cold-core eddy Jules and the continental shelf waters. However, $\partial T/\partial t - S$ (Plate 5c) exhibits a large-scale cooling of the continental shelf waters of ~1°C, which is not representative of advection, especially in that area where surface velocities are expected to be weak [*Rivas*, 1994]. Moreover, temperature variations associated with a temperature range of 10.5°-11.5°C reveal an important pattern of variability (Plate 5a). This is due to the fact that the continental shelf and the cold-core eddy waters are at the same temperature but exhibit different diurnal variations. Large errors in the representation of the source term could arise in such situations. A possible way to circumvent that drawback is to include a geographical parameter in the fit, say longitude, in order to dissociate the water masses from one another. We minimize the functional $\mathcal{G}'$:

$$\mathcal{G}'(T,\phi) = \left[\left(\frac{\partial T}{\partial t}\right) - \sum_{k=0}^{10}\sum_{l=0}^{10} a_{kl} T^k \phi^l\right]^2, \qquad (3)$$

where ϕ is longitude and a_{kl} are the polynomial coefficients. Again, the S field (Plate 5d) exhibits a general warming of the region; the main difference with the preceeding S field is observed in the cold-core ring and the continental shelf waters over which the heat gain is very large. The resulting $\partial T/\partial t - S$ field (Plate 5e) shall be used in the following to estimate advection.

3.3. Sensitivity of the Solution to Perturbations of the Source Term

Vigan et al. [this issue] perform a sensitivity study of the solution to perturbations of the influence of the constraints on divergence and vorticity in order to estimate an error of the velocity. One would like to include the sensitivity to perturbations of the source term also in the ellipses of covariance field so obtained. A possible way to do so is to perturb the coefficients of the polynomial relating $\partial T/\partial t$, T, and ϕ as shown in Figure 1 in the case of no geographic dependency. In the inversions performed in section 4 a sensitivity study of the solution associated with each representation of the source term is made. Among the 20 families of solutions estimated we keep the ones whose misfit to the

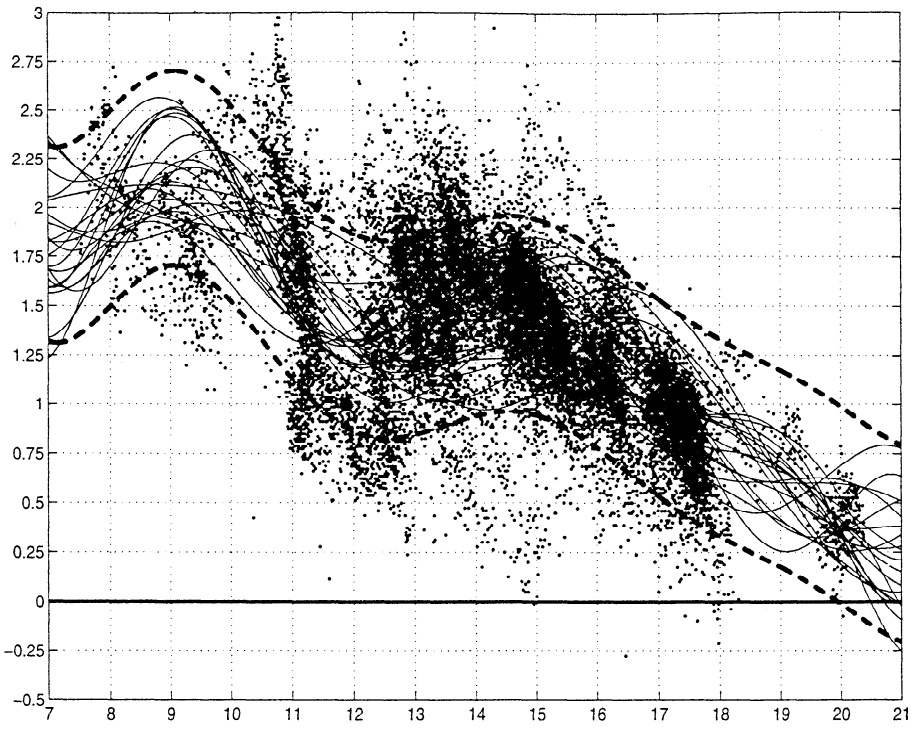

Figure 1. Family of polynomials (solid lines) obtained by performing 20 random perturbations on the coefficients superimposed on temperature time derivative as a function of temperature (black dots). The dashed lines correspond to the lower and upper bounds of the perturbations. The upper line is the sum of the polynomial and the error on the fit, and the lower line the difference.

heat balance is less than the minimum misfit plus 15% [*Vigan et al.*, this issue]. Variances and covariances are then computed on (u, v), yielding ellipses of covariance. These ellipses describe the sensitivity of the velocity to the influence of the constraints on divergence, vorticity, and the representation of the source term and provide a graphical representation of the estimated error on the solution.

4. Results

4.1. Results for the A Series

Inversions performed on the A series cover an area that surrounds the confluence (Plate 2a). Velocities over the continental shelf are not computed because temporal temperature variations there depend for a large part upon the source terms rather than upon advection as explained by *Vigan et al.*, [this issue]. The minimum reachable misfit value for image pair (A_3,A_4) is 9%. The resulting velocity field (Figure 2a) is the average of a family of acceptable solutions. That family stems from a sensitivity study described by *Vigan et al.* [this issue], for which the threshold of the misfit is chosen to be 15% greater than the minimum reachable misfit. The standard deviation of the velocity magnitude of the family of acceptable solutions provides an estimate of the error made on the magnitude. We obtain a rms value of 17% relative to 1660 perturbations performed on α, β, and the source term at misfit levels lower than 24%. The standard deviation of the direction of the acceptable velocity fields provides an estimate of the error made in direction. We obtain a rms value of 23°. Corresponding values of divergence and vorticity present an acceptable order of magnitude (10^{-6} and 10^{-5} s^{-1} respectively).

The main features of the surface flow observed encompass a recirculation cell centered at (36°S, 51°W) within the BC, a branching of the MC south of the Confluence at about (40°S, 55°W) and a strip centered on 39°S exhibiting low velocities between the two jets. Maximum surface velocities of 1.3 m s^{-1} are found at (38°S, 53°W). The velocities in the recirculation cell span $0.3 - 0.6$ m s^{-1} and $0.3 - 0.5$ m s^{-1} in the MC branching.

Results (Table 2) are compared to concomitant current meter velocity measurements. Note that the current meters closest to the surface are at a 350 m depth. Velocities estimated through the inversions are found to exhibit amplitudes 20% larger than the ones measured by the current meters (on average during the time step between the images A_3 and A_4) and directions 31° different. These differences are larger than the estimated error bar of 17% for the magnitude and 23° for the direction. However, surface velocities are probably some-

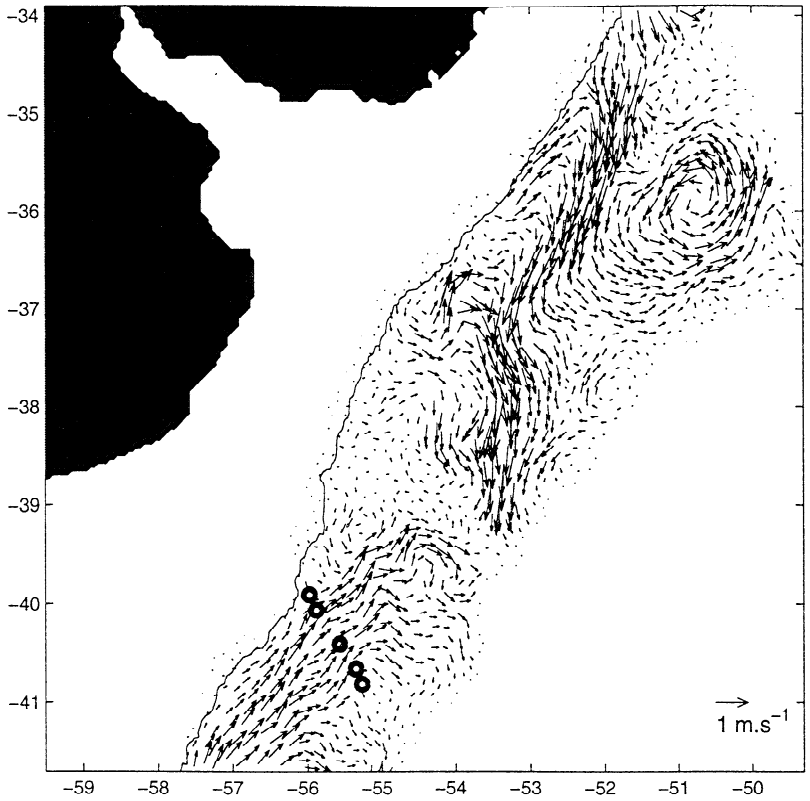

Figure 2a. Surface velocity field estimated through inversion of an 800x800 km subarea of image pair (A_3,A_4) of the A series. This field represents the average velocity of an acceptable family of solutions. Surface velocities reach 0.7 m s^{-1} in the Brazil Current, 0.6 m s^{-1} in the Malvinas Current and 1.3 m s^{-1} in the jet. The position of the current meter mooring array and the 200 m isobath are superimposed.

what greater than those at 350 m. The A series spans the period from March 18 to March 22, 1995, at the end of austral summer. A sharp and shallow (few tens of meters) seasonal thermocline is formed during that period of the year on top of the MC [*Provost et al.*, 1996]. Assuming an average vertical shear on the horizontal velocity of $2.5 - 3\ 10^{-4}$ s^{-1} [*Vivier and Provost*, 1999a], a 0.6 m s^{-1} velocity magnitude at the surface yields a 0.5 m s^{-1} velocity magnitude at a 350 m depth, that is to say, a 17% difference: the overestimate of 20% of the velocity obtained by inversion can be so explained.

4.2. Results for the B Series

Inversions performed on the B series are centered on the warm-core eddy Léon event (Plate 2b). The minimum reachable misfit value estimated for image pair (B_1,B_2) is 13%. The velocity field from image B_1 to B_2 (Figure 3a) exhibits an energetic vortex at the center of the region and another one to the southeast. The estimate of the error represented by ellipses of covariance (Figure 3b) made on the magnitude of the velocity is 14% rms relative to 2720 perturbations performed on α, β, and the source term at misfit levels <28%. The estimate of the error in direction is 19°.

The surface flow is dominated by two eddies: warm-core eddy Léon detaching from the BC overshoot with azimuthal velocities as high as 1.2 m s^{-1} and an eddy structure to the southeast of eddy Léon exhibiting azimuthal velocities of 0.9 m s^{-1}. Eddy Léon is slowly moving to the north at $\sim$ 0.02 m s^{-1}. As frequently observed in warm-core rings [*Olson*, 1980], the maximum azimuthal velocity is not found on the edge of the warm patch but rather slightly inside. The eddy structure to the southeast comprises two water masses: a cold one to the northeast (4°C) and a warmer one to the southwest (12°C). Surface velocities of $0.3 - 0.7$ m s^{-1} are found in the overshoot.

Statistics on the inversions (Table 3) are the same as in Table 2 except that there are unfortunately no *in situ* velocity measurements acquired in warm-core eddy Léon. However, the results obtained are compared with sea surface geostrophic velocity anomaly profiles from TOPEX/Poseidon. Track 239 intersects the eddy on September 28, 1995 (Figure 3a). A 35 km low-pass filter is applied to the height anomaly before derivation of the geostrophic velocity anomaly. We project the velocity estimated through the inversion orthogonally along the altimeter track and apply a 35 km low-pass

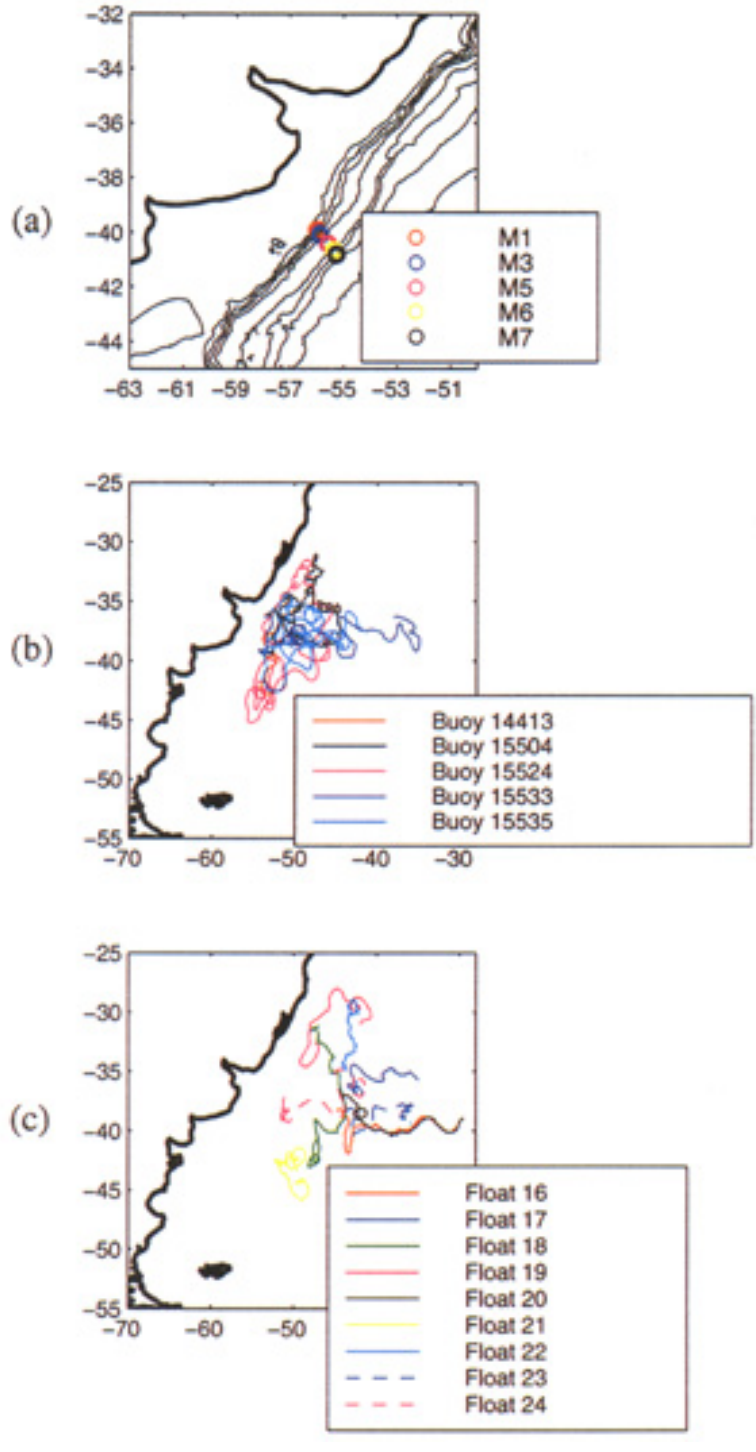

Plate 3. (a) Current meter mooring array location. (b) Surface trajectories of five Marisonde buoy deployed in the confluence area from June 25, 1995, to December 31, 1995. (c) Trajectories of the nine RAFOS floats after they surface on November 10, 1995, up to December 31, 1995 (end of the advanced very high resolution radiometer (AVHRR) series).

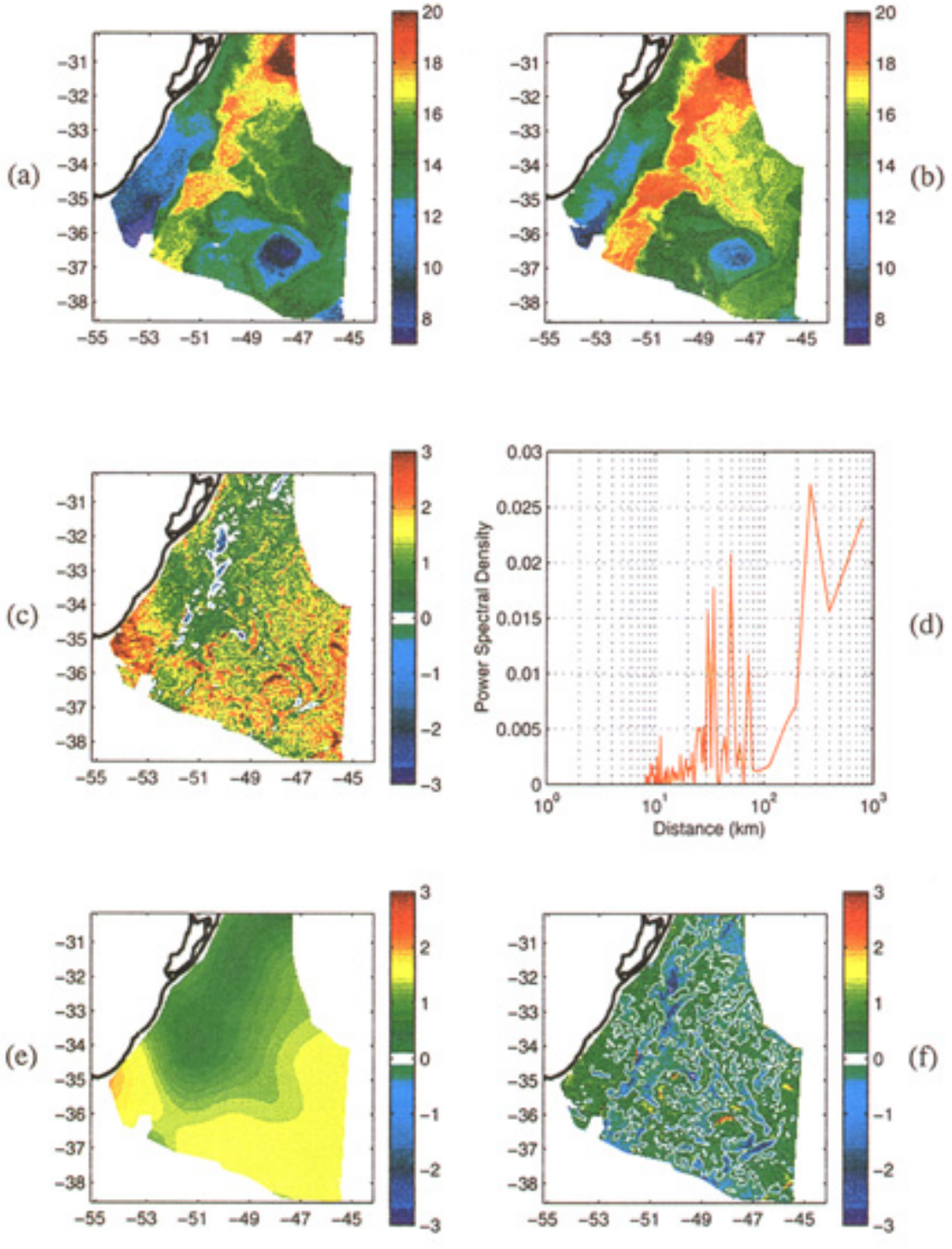

Plate 4. (a) and (b) Images D_1 and D_2 of the D series. (c) Temperature variations from the first to the second image. (d) Power spectral density of the zonal average of Plate 4c. (e) Source term S obtained by low-pass filtering Plate 4c. (f) Temperature variations attributed to advection.

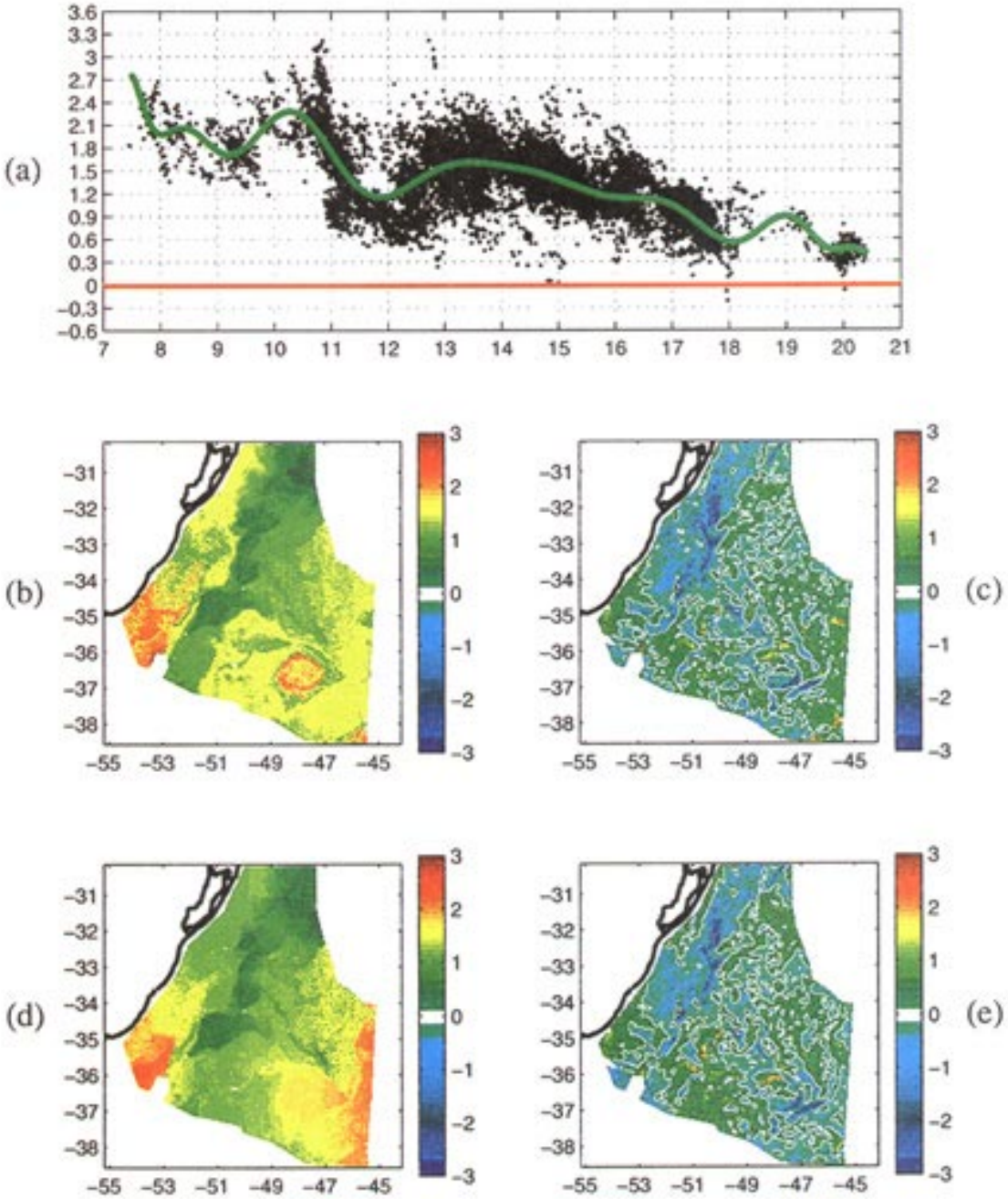

Plate 5. (a) Scatter plot of temperature variations as a function of the average temperature of image pair (D_1,D_2). The polynomial resulting from the fit is superimposed. (b) Source term S obtained by fitting the polynomial to $\partial T/\partial t$ as a function of temperature. (c) Temperature variations after removing the source term. (d) Source term S obtained by fitting the polynomial to $\partial T/\partial t$ as a function of temperature and longitude. (e) Temperature variations after removing the source term.

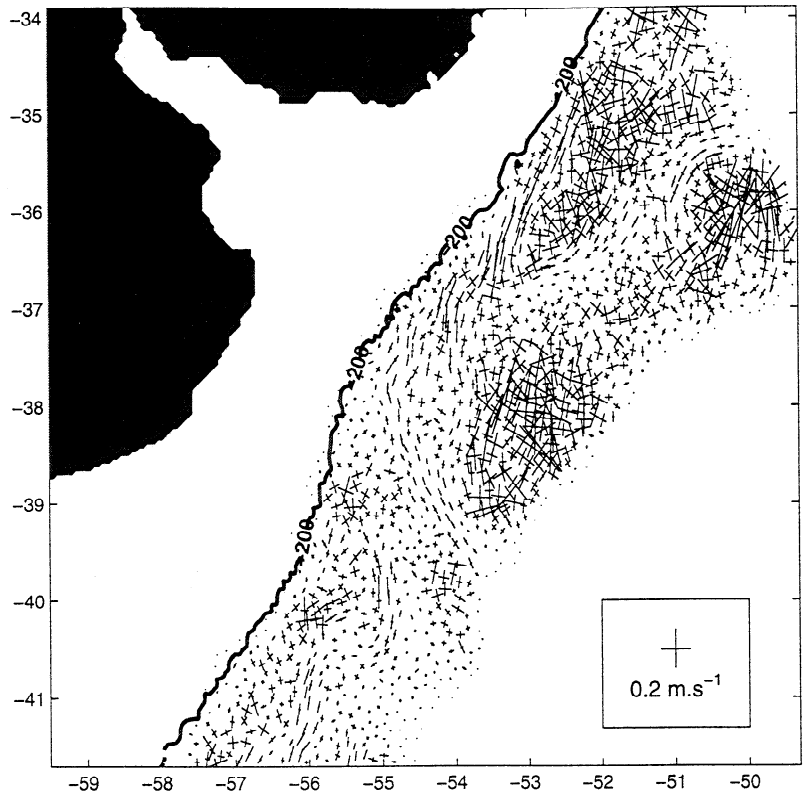

Figure 2b. Field of ellipses of covariance associated with the velocity field, estimated by performing 1660 perturbations on α, β, and the source term at misfit levels ϵ <24%. We can observe the sensitivity of the solution to perturbations of the divergence and vorticity constraints over regions where the larger axis is much larger than the smaller one, typically in the jets. Regions where the solution is sensitive to the source term are characterized by open ellipses, in the Brazil and the subtropical waters. The estimate of the error is 18% in magnitude of the velocity and 23° in direction.

filter to make both signals comparable. A 35% rms error for concomitant image pair (B_1,B_2) is obtained between both velocity profiles (overestimate). That value is much greater than the error bar of 14% estimated for the magnitude. One reason for that relatively large error is that the velocity anomalies obtained from altimetry may differ significantly from the absolute velocity, especially because of a probably large contribution of ageostrophy.

4.3. Results for the C Series

Inversions performed on the C series are centered on the BC overshoot (Plate 2c). Concomitant 3 day Marisonde drifting buoys and RAFOS float trajectories are superimposed on the velocity field from image C_7 to C_8 (Figure 4a). They represent 3 day trajectories, the end position of which is marked by a circle and corresponds to the date of the inversion. Ellipses

Table 2. Results on the Inversions Performed on the A Series

Image Pair	Minimum Misfit, %	v_{max}, m s^{-1}	$\lvert\bar{D}\rvert$, 10^{-6}s^{-1}	$\lvert\zeta\rvert$, 10^{-5}s^{-1}	E_{Norm}, %	$E_{Direction}$, deg
(A_1,A_2)	10	1.1	0.9	1.0	19.0	23.4
(A_2,A_3)	13	1.1	1.0	0.8	22.1	33.0
(A_3,A_4)	9	1.3	0.9	0.6	21.3	37.4
(A_4,A_5)	12	1.2	1.0	1.4	30.6	35.9
(A_5,A_6)	15	1.2	0.9	0.6	14.3	24.1
(A_6,A_7)	9	0.9	0.9	0.7	-	-
Average	11	1.1	0.9	0.8	21.5	30.8

Minimum misfit, maximum velocity, mean absolute divergence, mean absolute vorticity, rms error in magnitude, and direction of the velocity from current meter data.

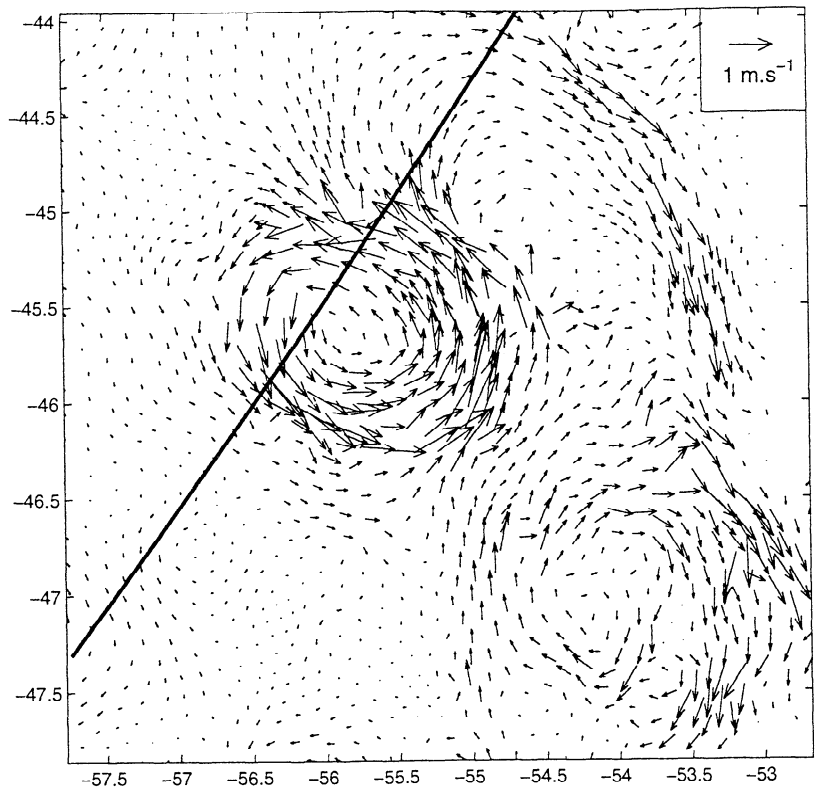

Figure 3a. Surface velocity field estimated through inversion of a 400x400 km subarea of image pair (B_1,B_2) of the B series. Surface velocities of 1.2 m s^{-1} are obtained in warm-core eddy Léon. Track 239 of TOPEX/Poseidon is superimposed.

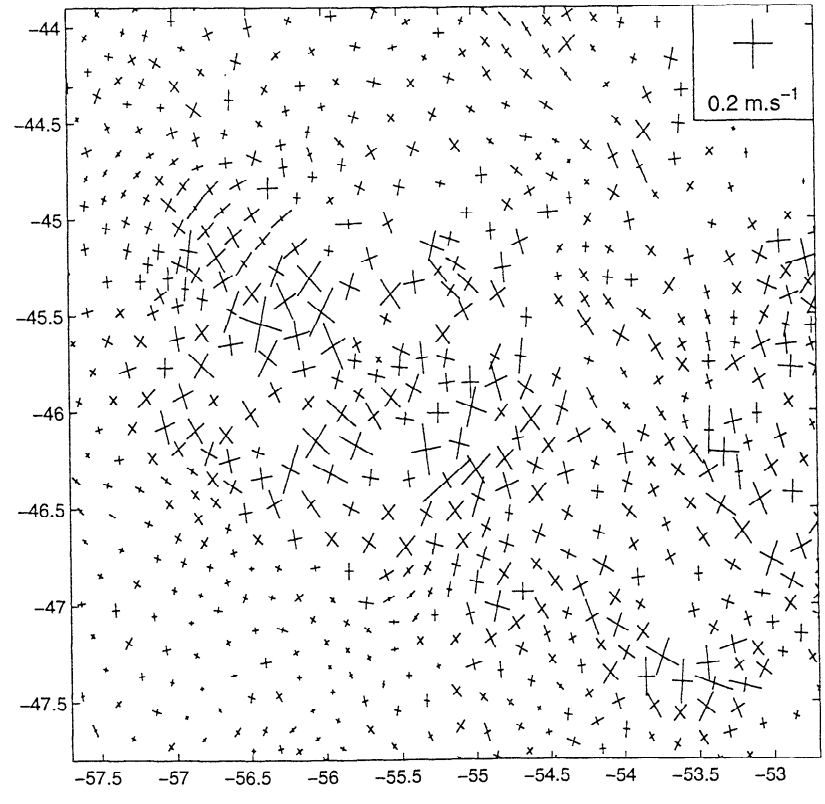

Figure 3b. Ellipses of covariance field estimated by performing 2720 perturbations on α, β, and the source term at misfit levels <28%. The estimate of the error is 14% in magnitude of the velocity and 19° in direction.

Table 3. Results on the Inversions Performed on the B Series

Image Pair	Minimum Misfit, %	v_{max}, m s^{-1}	$\|D\|$, 10^{-6}s^{-1}	$\|\zeta\|$, 10^{-5}s^{-1}	E_{Norm}, %
(B_1,B_2)	13	1.2	1.4	0.9	-
(B_2,B_3)	13	1.2	1.0	0.6	35%
(B_3,B_4)	9	1.0	0.8	0.5	-
(B_4,B_5)	17	0.8	0.9	0.6	-
(B_5,B_6)	17	1.0	1.0	0.7	-
(B_6,B_7)	14	0.7	0.7	0.5	-
(B_7,B_8)	23	0.9	1.5	0.8	-
Average	15	1.0	1.0	0.7	-

Minimum misfit, maximum velocity, mean absolute divergence, mean absolute vorticity, and rms error in magnitude of the velocity with TOPEX/Poseidon geostrophic velocity anomaly along track 239.

of covariance (Figure 4b) are computed on the basis of perturbing α, β, and the source term at misfit levels lower than 43%. There are 2680 velocity fields used for the sensitivity study. The rms error in magnitude is estimated to be 16%. The estimate of the error in the direction of the velocity is 29°.

We obtain through the inversion of image pair (C_7,C_8) a jet velocity at the meander entrance at (36°S, 52°W) as high as 1.3 m s^{-1} decreasing downstream to 1.2 m s^{-1} at (39.5°S, 52°W) and to 0.9 m s^{-1} at (41.5°S, 48.5°W). The recirculation cell centered at (39°S, 50.5°W) exhibits velocities of 0.3 – 0.6 m s^{-1}. The northeastern part of a large warm eddy is observed at (41°S, 53.5°W), with velocities of the order of 0.6 m s^{-1}. Finally, a smaller and cooler eddy is found at (38.2°S, 53.2°W) where velocities are of the order of 0.4 m s^{-1}.

Comparisons to *in situ* velocity measurements (Table 4) yield a 9% rms error (underestimation) on the

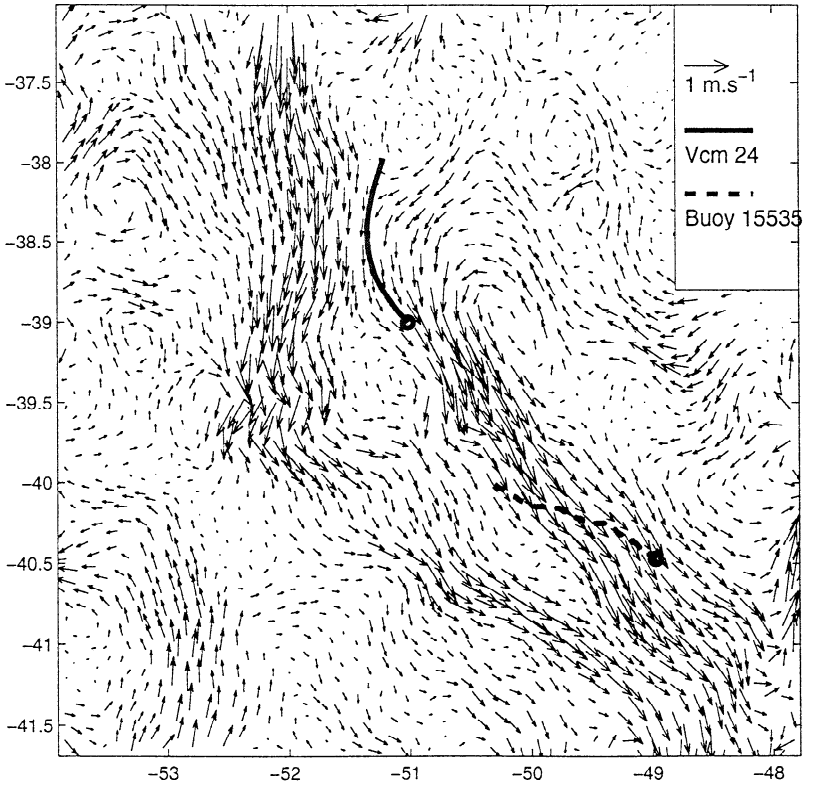

Figure 4a. Surface velocity field estimated through inversion of a 500x500 km subarea of image pair (C_7,C_8) of the C series. Surface velocities of 0.6 m s^{-1} are obtained in the Brazil Current, 0.8 m s^{-1} in the Malvinas Current, and up to 1.3 m s^{-1} in the Brazil Current overshoot. The trajectory of Marisonde buoy 15535 and RAFOS float 16 are superimposed on the velocity field.

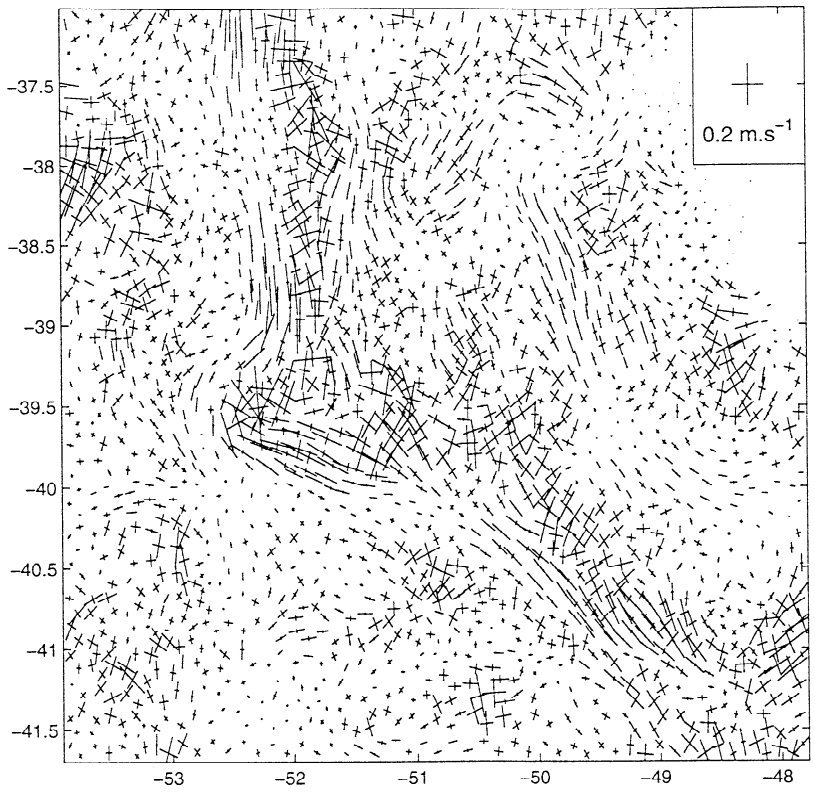

Figure 4b. Ellipses of covariance field estimated by performing 2680 perturbations on α, β, and the source term at misfit levels <43%. The estimate of the error is 16% in magnitude of the velocity and 29° in direction.

magnitude of the velocity and an 11° rms error on the direction. These values are well within the error bars stemming from the sensitivity study, which are 16% for the magnitude and 29° for the direction.

4.4. Results for the D Series

Inversions performed on the D series are centered on the BC and cold-core eddy Jules (Plate 2d). The 3 day concomitant buoys and float trajectories are superimposed on the estimated velocity field (Figure 5a). Ellipses of covariance (Figure 5b) are computed by performing 1860 perturbations on α, β, and the source term at misfit levels lower than 25%. The estimated error in magnitude is 20% rms. The estimated error in direction is 33°.

In the BC, velocities are of the order of 0.4 m s^{-1} except over the southernmost eddy centered at (36.5°S,

Table 4. Results on the Inversions Performed on the C Series

Image Pair	Minimum Misfit, %	v_{max}, m s^{-1}	$\lvert D\rvert$, 10^{-6}s^{-1}	$\lvert\zeta\rvert$, 10^{-5}s^{-1}	E_{Norm}, %	$E_{Direction}$, deg
(C_1,C_2)	22	1.2	1.0	0.7	9.1	10.2
(C_2,C_3)	32	0.9	0.6	0.4	11.3	8.6
(C_3,C_4)	14	0.9	2.4	1.8	7.0	8.9
(C_4,C_5)	14	1.2	1.2	0.8	10.5	21.7
(C_5,C_6)	19	0.6	0.6	0.4	37.3	44.1
(C_6,C_7)	10	1.0	0.9	0.6	13.2	5.3
(C_7,C_8)	28	1.3	1.2	0.9	9.3	10.8
(C_8,C_9)	17	1.5	0.9	0.8	9.8	11.2
Average	20	1.1	1.1	0.8	13.4	15.1

Minimum misfit, maximum velocity, mean absolute divergence, mean absolute vorticity, rms error in magnitude, and direction of the velocity from Marisonde buoys and RAFOS floats.

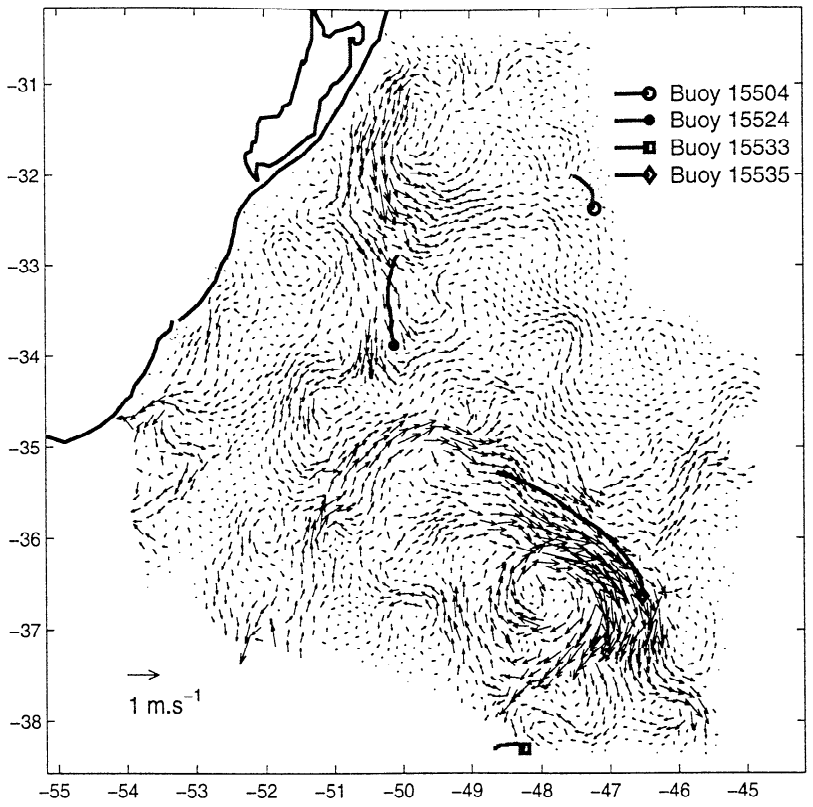

Figure 5a. Surface velocity field estimated through inversion of an 870x870 km subarea of image pair (D_1,D_2) of the D series. Surface velocities of 0.8 m s^{-1} are obtained in the Malvinas Current, 0.4 m s^{-1} are obtained in the Brazil Current, and up to 1.3 m s^{-1} are obtained on the periphery of cold-core eddy Jules. Several buoys and floats were trapped in the area: their tracks are superimposed on the velocity field.

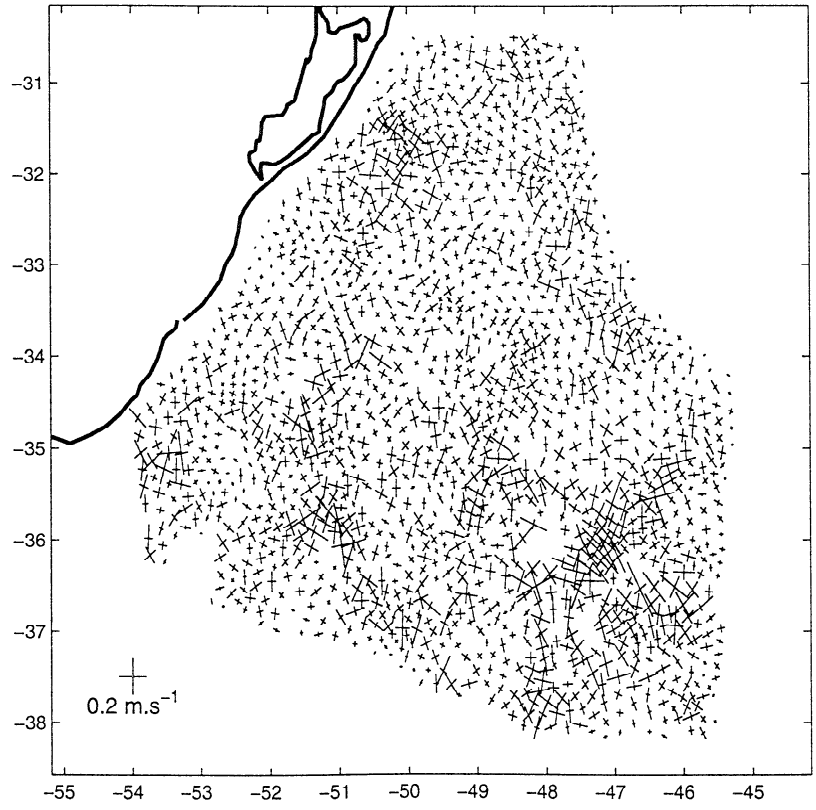

Figure 5b. Ellipses of covariance field estimated by performing 1860 perturbations on α, β, and the source term. The misfit level is 25%. The estimate of the error is 20% in magnitude of the velocity and 33° in direction.

Table 5. Results on the Inversions Performed on the D Series

Image Pair	Minimum Misfit, %	v_{max}, m s^{-1}	$\|D\|$, $10^{-6}s^{-1}$	$\|\zeta\|$, $10^{-5}s^{-1}$	E_{Norm}, %	$E_{Direction}$, deg
(D_1,D_2)	10	1.3	2.1	1.3	7.2	28
(D_2,D_3)	18	1.2	1.8	0.9	15.1	12
Average	14	1.2	2.0	1.1	11.2	20

Minimum misfit, maximum velocity, mean absolute divergence, mean absolute vorticity, rms error in magnitude, and direction of the velocity from Marisonde buoys and RAFOS floats.

52°W) where velocities as high as 0.8 m s^{-1} are found. Cold-core eddy Jules exhibits velocities of the order of 0.8 m s^{-1}.

Comparisons of the velocity estimates with available concomitant *in situ* data (Table 5) yield a 7% error in magnitude and a 20° error in direction. These values are well within the error bars of 20% for the magnitude and 33° for direction stemming from the sensitivity study.

5. Transports

With hypothesis on the vertical structure of the current, transport estimates can, in principle, be computed from estimates of surface velocities. The MC has been recently examined in the light of a currentmeter mooring array [*Vivier and Provost,* 1999a]. With an uncertainty in the vertical structure and taking into account error bars associated with surface velocity estimates, what kind of uncertainty can be estimated on the transport ?

First, we make the assumption that the velocity magnitudes below the surface are less than or equal to that at the surface [*Vivier and Provost,* 1999a]. Second, we assume that the depth of the interface between the MC and the Antarctic Intermediate Water (AAIW) waters is 1500 m on the basis of the same observations. Third, we suppose that the water velocity at the base of the MC is equal to one fifth of the surface velocity at least and equal to the velocity at the surface at most. A lower bound for the transport is defined with a linear vertical velocity profile from the surface to the base of the MC and a minimum velocity at the surface (velocity obtained by inversion minus the error bar) (Figure 6). We define an upper bound of the MC transport assuming a constant velocity as a function of depth (barotropic case) and a maximum velocity at the surface (velocity obtained by inversion plus the error bar). The transport is estimated as the average of both values and the error bar as half of the difference.

That simple model is applied to a subarea of the summer image series (A) centered on the MC. Transports are computed across transects perpendicular to the surface flow along the 1000 m isobath (Figure 7a). The transects across which these values are obtained are bounded to the west by the 200 m isobath and to the

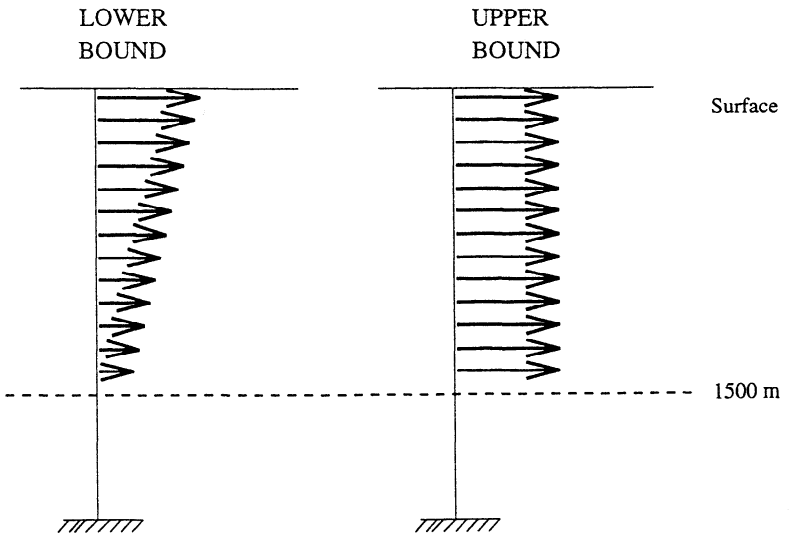

Figure 6. Vertical velocity profiles of the MC. A minimum transport value is computed assuming a linear velocity profile down to 1500 m. A maximum value is estimated assuming a constant velocity as a function of depth.

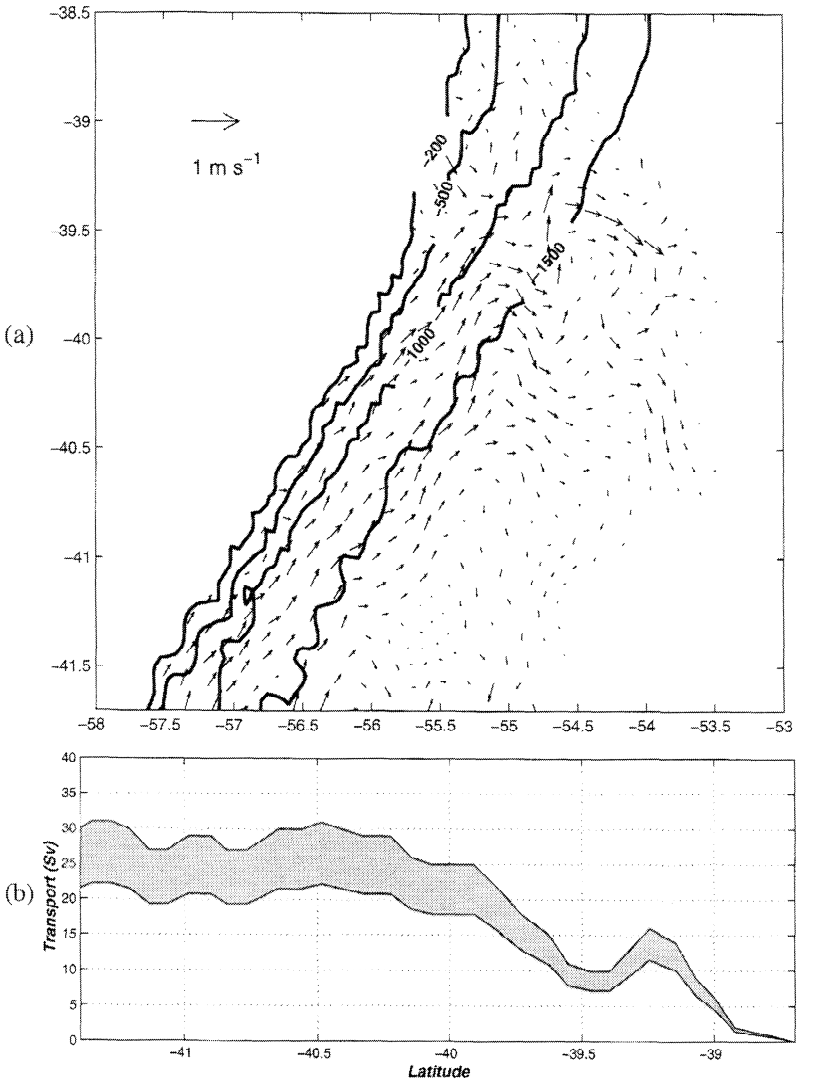

Figure 7. (a) Velocity field of Figure 2a centered on the MC. (b) Transport of the MC (sverdrups) on March 10, 1995, along the 1000 m isobath. Transports are computed across sections perpendicular to the MC flow and bounded by the 9°C isotherm and the 200 m isobath.

east by the 9°C isotherm. Values are of the order of 25-30 Sv. From 41.5° to 40°S the MC transport decreases from 25 ± 5 to 20 ± 5 *Sv* (Fig. 7b). Farther north, an abrupt change can be observed between 40° and 38°S where the transport decreases from $\sim 20 \pm 5$ *Sv* to zero. That may be explained by the fact that the MC returns to the south at these latitudes. These values are in agreement with *Vivier and Provost* [1999b], who estimated the MC transport with TOPEX/Poseidon data.

6. Discussion and Conclusions

Sea surface velocity fields are estimated over the Brazil-Malvinas Confluence region from sequences of SST images. Inversions are performed on four image series over which typical oceanic surface patterns are observed, as the BC and the MC, the BC overshoot and the MC return flow, warm and cold core eddies, and recirculation cells of the BC and the MC. The velocity magnitudes obtained are 0.5-0.6 m s^{-1} in the MC and 0.3-0.7 m s^{-1} in the BC. For the four image series the velocity is relatively steady in the MC, and a stronger variability is observed in the BC. That observation is in agreement with the general knowledge of the area [*Gordon*, 1989; *Peterson and Stramma*, 1991; *Provost et al.*, 1995; *Maamaatuaiahutapu et al.*, 1994; *Garzoli and Garaffo*, 1989]. Very high velocities of up to 1.5 m s^{-1} are estimated with the C series in the BC overshoot. The study of warm-core eddy Léon reveals that the structure is very energetic with velocities of the order of 1 m s^{-1}. Inversions performed on the D series show that cold-core eddy Jules is also a very energetic structure, fitting in with the results of *Escoffier et al.* [1998].

The relatively good results obtained must not direct our attention away from the limitations of the method.

First of all, a high spatiotemporal variability of SST is necessary for such an application. Western boundary regions meet that condition but are massively cloud-covered. As mentioned in section 2, only 27 images are usable out of 838 for the whole high resolution picture transmission (HRPT) series. Second, the representation of the source term involved in the heat balance stems from the SST and a geographical parameter, which is a very simplistic approach. Obviously, heat fluxes as well as entrainment do not depend solely upon such quantities. Nevertheless, sensitivity studies tend to show that the inversions do not depend so much upon the source term, rather upon the penalization of divergence and vorticity.

The velocity fields estimated are in good quantitative agreement with the *in situ* measurements obtained by the Marisonde buoys and the RAFOS floats. On average for the four series the error in magnitude is 15% and in direction is 22°, which is an improvement compared to previous quantitative results on the topic [*Kelly*, 1989; *Kelly and Strub*, 1992; *Kelly*, 1994]. These results are heightened by the sensitivity studies because the error fields estimated exhibit higher magnitudes than the difference with *in situ* measurements. However, the differences computed for the A and B series relative to current meters and altimetric measurements are greater than the predicted error. It is likely, though, that velocities at 350 m are lower than that at the surface, especially during summer periods when a seasonal thermocline of a few tens of meters is observed at the surface over the MC. The large difference between the velocities estimated for the B series by inversion and TOPEX/Poseidon geostrophic velocity anomalies is probably due to the fact that the altimeter yields a velocity anomaly as the inverse model tends to estimate absolute velocities. Transports are computed in the last section across the MC. The order of magnitude obtained is ~25 Sv between 41° and 40°S. That value is in agreement with recent transport estimates in that region over the same period of time.

Acknowledgments. This work could not have been possible without Maxence Revault d'Allonnes. We are greatful to Don Olson for his helpful comments. We thank Keitapu Maamaatuaiahutapu for his numerous suggestions. X. Vigan and C. Provost were supported by PNTS (programme National de Télédétection Spatiale) and by the PNEDC-WOCE (Programme National d'Étude du Climat). The AVHRR imagery used in this study was recorded by the National Meteorological Service of Argentina as part of the collaboration agreement with the University of Miami. We thank Joanie Splain for processing the SST fields and Jim Brown. Marisonde buoys data were processed at Météo France in Brest by Pierre Blouch. We are greatful to Antonio Lourenço for providing the RAFOS float trajectories.

References

Cornillon, P., and L. Stramma, The distribution of diurnal sea surface warming events in the western Sargasso Sea, *J. Geophys. Res., 90,* 11,811-11,815, 1985.

Emery, W. J., J. Brown, and Z. P. Nowak, AVHRR image navigation: Summary and review, *Photogramm. Eng. Remote Sens., 55,* 1175-1183, 1989.

Escoffier, C., Sur le forçage atmosphérique et la formation des eaux modales subtropicales dans l'Atlantique Sud-Ouest, PhD. thesis, 302 pp., Univ. Paris VI, Paris, 1998.

Garzoli, S. L., and Z. Garaffo, Transports, frontal motion and eddies at the Brazil-Malvinas Confluence, *Deep Sea Res. Part I, 36,* 681-703, 1989.

Gordon, A. L., Brazil-Malvinas Confluence: 1984, *Deep Sea Res. Part I, 36,* 359-384, 1989.

Hooker, S. B., and J. W. Brown, Dipole rings and vortex interactions of the Brazil Current, *IEEE Trans. Geosci. Remote Sens., 34,* 1323-1330, 1996.

Kartavtseff, A., Bouées Marisondes dans la région de Confluence Brésil-Malouines, *Tech. Rep.,* 90 pp., Lab. d'Océanogr. et de Climatol., Paris, 1996.

Kelly, K. A., An inverse model for near-surface velocities from infrared images, *J. Phys. Oceanogr., 19,* 1845-1864, 1989.

Kelly, K. A., Reply, *J. Geophys. Res., 99,* 10,301, 1994.

Kelly, K. A., and P. T. Strub, Comparision of velocity estimates from advanced very high resolution radiometer in the coastal transition zone, *J. Geophys. Res., 97,* 9653-9668, 1992.

Lourenço, A., Positionnement de flotteurs sous-marins par méthode acoustique, Ph.D. thesis, 117 pp., Conservatoire Natl. des Arts et Métiers, Paris, 1997.

Maamaatuaiahutapu, K., V. Garçon, C. Provost, M. Boulahdid, and A. Bianchi, Spring and water mass composition in the Brazil-Malvinas Confluence, *J. Mar. Res., 52,* 397-426, 1994.

McClain, E. P., W. P. Pichel, and C. C. Walton, Comparative performance of AVHRR-based multichannel sea surface temperature, *J. Geophys. Res., 90,* 11,587-11,601, 1985.

Olson, D., The physical oceanography of two rings observed by the Cyclonic Ring Experiment, *J. Phys. Oceanogr., 10,* 514-527, 1980.

Olson, D., G. Podesta, R. H. Evans, and O. Brown, Temporal variations in the separation of Brazil and Malvinas Currents, *Deep Sea Res. Part I, 35,* 1971-1990, 1988.

Peterson, R. G., and L. Stramma, Upper-level circulation in the South Atlantic Ocean. *Prog. Oceanogr., 26,* 1-73, 1991.

Provost, C., S. Gana, V. Garçon, K. Maamaatuaiahutapu, and M. England, Hydrographic conditions in the Brazil-Malvinas Confluence during austral summer 1990, *J. Geophys. Res., 100,* 10,655-10,698, 1995.

Provost, C., V. Garçon, and L. M. Falcon, Hydrographic conditions in the surface layers over the slope-open ocean transition area near the Brazil-Malvinas Confluence during austral summer 1990, *Cont. Shelf. Res., 16,* 215-235, 1996.

Rivas, A. L., Spatial variation of the annual cycle of temperature in the Patagonian shelf between 40 and 50° of south latitude, *Cont. Shelf. Res., 14,* 1539-1554, 1994.

Saunders, P. M., and B. A. King, Oceanic fluxes on the WOCE A11 section, *J. Phys. Oceanogr., 25,* 1942-1958, 1994.

Stramma, L., P. Cornillon, R. A. Weller, J. F. Price, and M. G. Briscoe, Large diurnal sea surface temperature variability: Satellite and *in situ* measurements, *J. Phys. Oceanogr., 16,* 827-837, 1986.

Vigan, X., C. Provost, R. Bleck, and P. Courtier, Sea surface velocities from sea surface temperature image sequences, 1, Method and validation using primitive equation model output, *J. Geophys. Res.,* this issue.

Vivier, F., and C. Provost, Direct velocity measurements

in the Malvinas Current, *J. Geophys. Res., 104*, 21,083-21,104, 1999a.

Vivier, F., and C. Provost, Volume transport of the Malvinas Current. Can the flow be monitored by T/P, *J. Geophys. Res., 104*, 21,105-21,122, 1999b.

G. Podesta, Rosentiel School of Marine and Atmospheric Sciences, University of Miami, Miami, FL 33149.

C. Provost and X. Vigan, Laboratoire d'Océanographie Dynamique et de Climatologie, Centre National de la Recherche Scientifique, 75005 Paris, France.
(Xavier.Vigan@lodyc.jussieu.fr)

(Received May 28, 1999; revised January 12, 2000; accepted January 24, 2000.)